

Figure 1

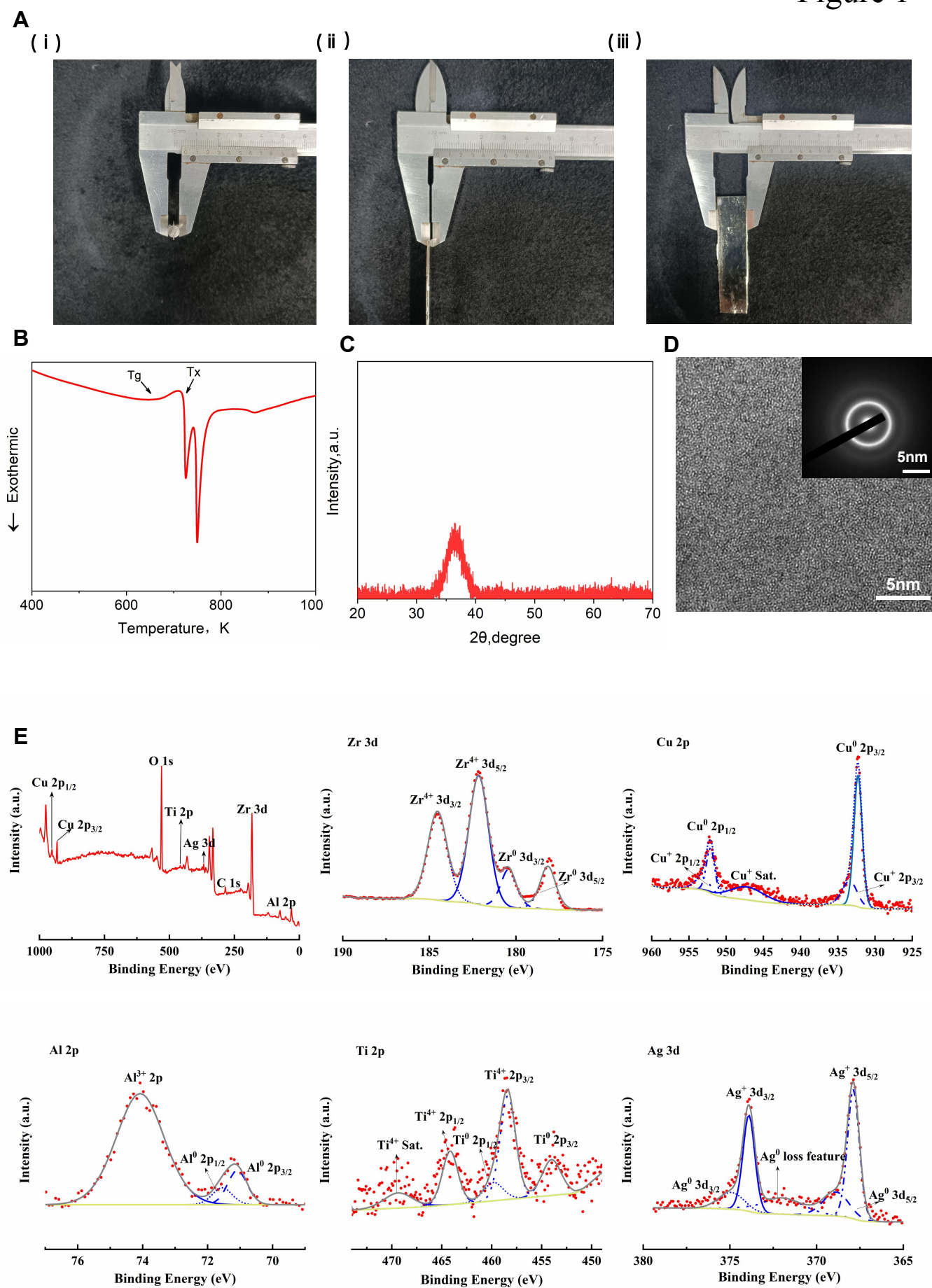


Figure 1: Structural properties, thermal parameters and surface chemical compositions

A. Representative photographs of the Zr-BMG sample showcase various dimensions: i. and ii. depict rectangular specimens measuring 16mm in width and 1mm in thickness, while iii. presents a cylindrical sample with a diameter of 5mm.

B. Representative differential scanning calorimetry (DSC) data of $\text{Zr}_{61}\text{Cu}_{23}\text{Al}_{12}\text{Ti}_2\text{Ag}_2(\text{at.}\%)$ (Zr-BMG), showing their transition temperature (T_g), crystallization temperature (T_x), and supercooled liquid region (ΔT).

C. Representative X-ray Diffraction (XRD) curve illustrates a distinctive "bread-loaf" peak, characteristic of the non-crystalline or amorphous structure inherent to the Zr-BMG material.

D. Representative transmission Electron Microscopy (TEM) image shows microstructural homogeneity and the amorphous ring.

E. Representative X-ray Photoelectron Spectroscopy (XPS) curve presents both the survey spectrum and elemental sub-spectra, affirming the compositional consistency of the Zr-BMG sample with the intended elements. The oxide film formed on the surface of Zr-BMG consisted of ZrO_2 , Al_2O_3 . Cu were mainly presented as a metal form beneath the oxide layer. Ag mainly exists in the form of free silver ions.

Figure 2

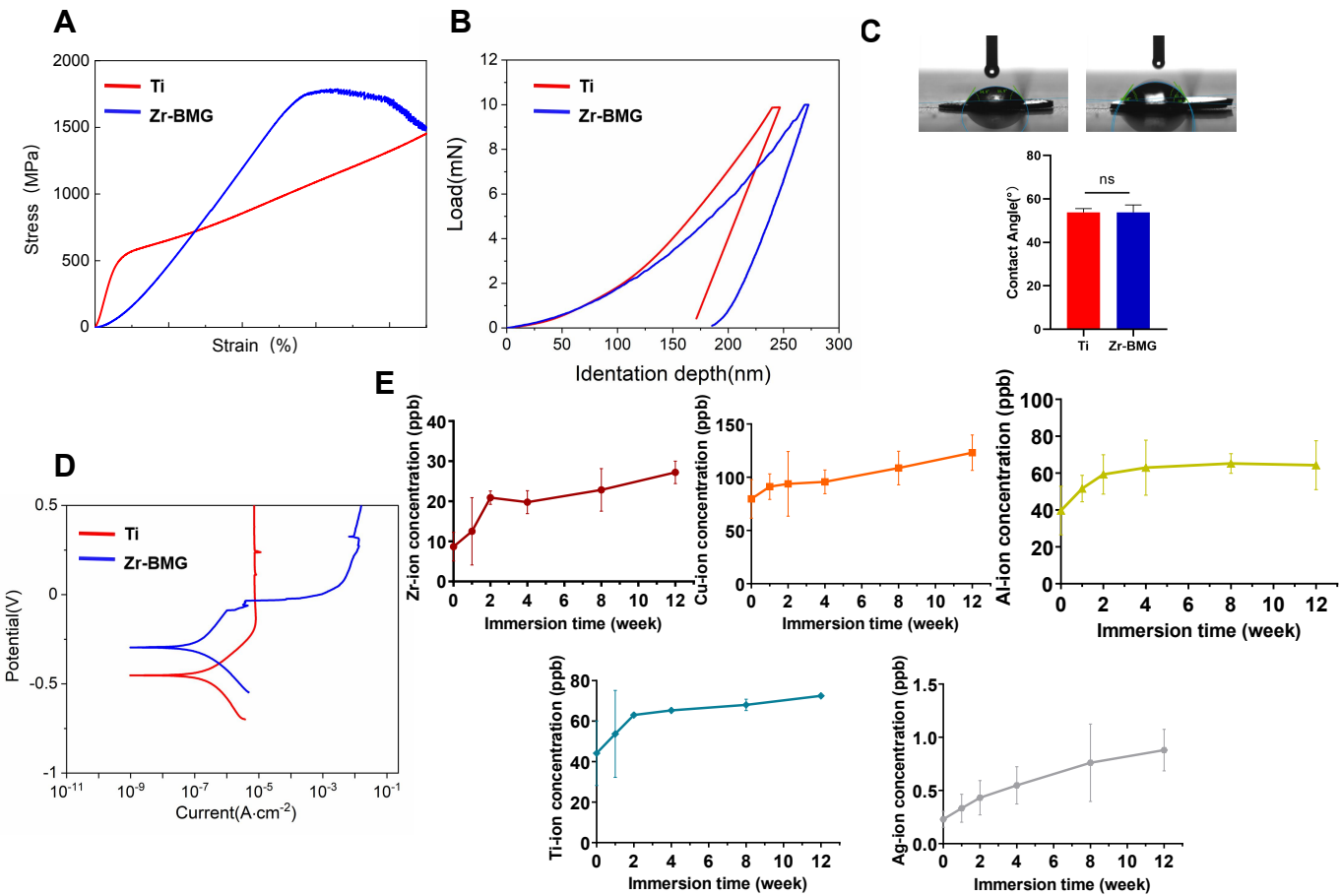


Figure 2 Mechanical properties and electrochemical results.

A. Compression stress-strain curves show Zr-BMG significantly surpassing Ti.

B. Load-displacement curves of all samples at indentation load of 10mN.

C. Representative images of contact angle measurements with simulated body fluid (SBF) on the surfaces of Ti and Zr-BMG. Statistical analysis indicates no significant difference between the two materials in terms of surface wettability.

E. Potentiodynamic-polarization curves and corrosion parameters of all samples in simulated body fluid (SBF), indicating a slower corrosion rate of Zr-BMG compared to cpTi.

G. The release of different metal ions in SBF at 37°C measured by ICP-MS. The release of various metal ions from Zr-BMG stabilizes after 2 weeks in the simulated body fluid environment.

Data are presented as mean±SD. * $p<0.05$, ** $p<0.01$ and *** $p<0.001$.

Figure 3

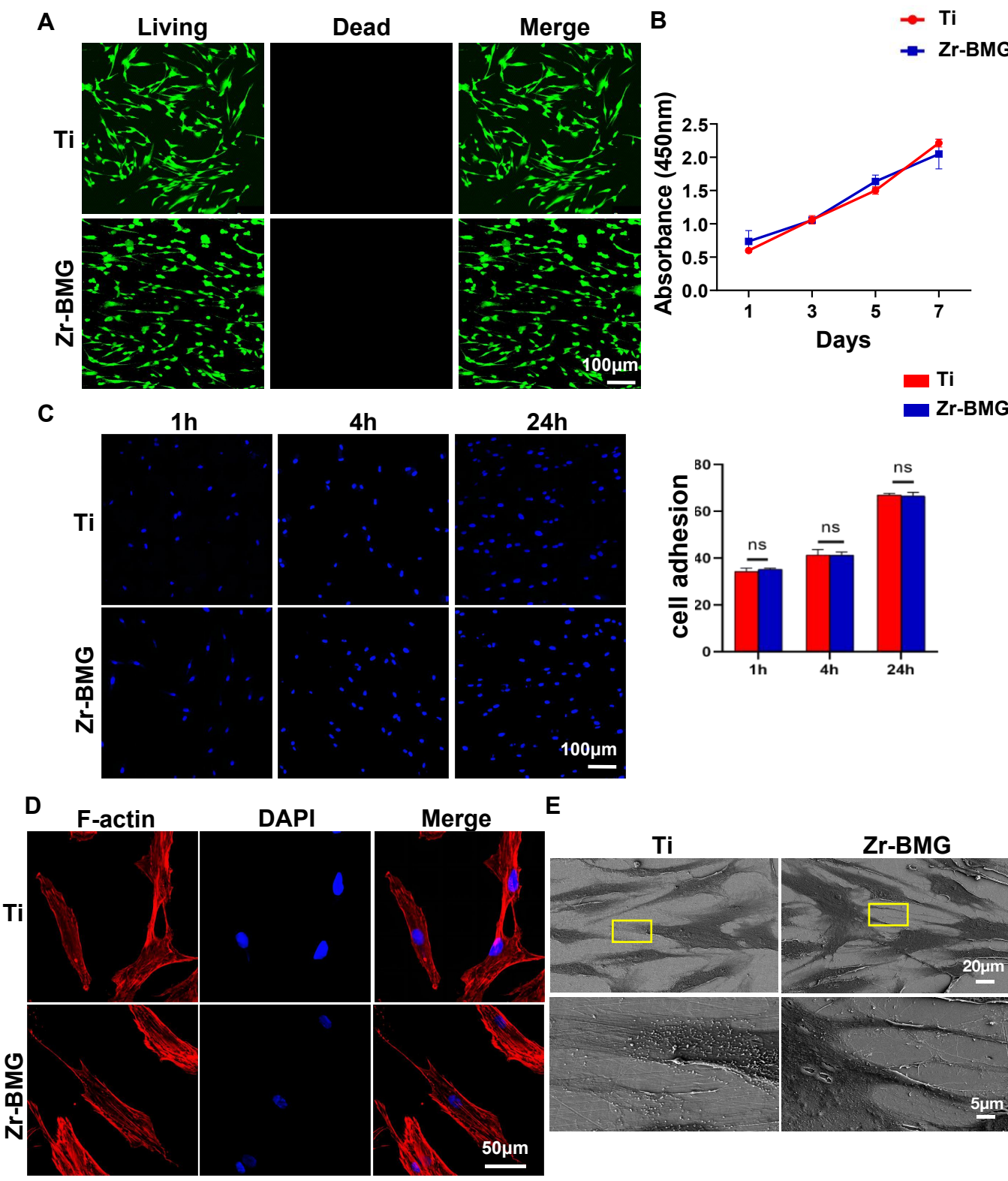


Figure 3 Cell viability ,cell adhesion and cell morphology features.

A. Fluorescent staining images after 1, 4, and 24 hours of cell culture, presenting the results of cell proliferation and viability, indicating minimal cytotoxicity differences between Zr-BMG and Ti.

B. The CCK-8 assay results, revealing similar cell proliferation rates on Zr-BMG and Ti surfaces at intervals of 1, 3, 5, and 7 days.

C. Left: Representative cell adhesion figures and cell number counts at 1h, 4h, and 24h. Right: Statistical analysis confirmed no significant difference between the two.

D. Phalloidin staining of hJBMMSCs F-actin at 24h.

E. SEM images of hJBMMSCs cell morphology on material surface at 24h.

Data are presented as mean \pm SD. * p <0.05, ** p <0.01 and *** p <0.001.

Figure 4

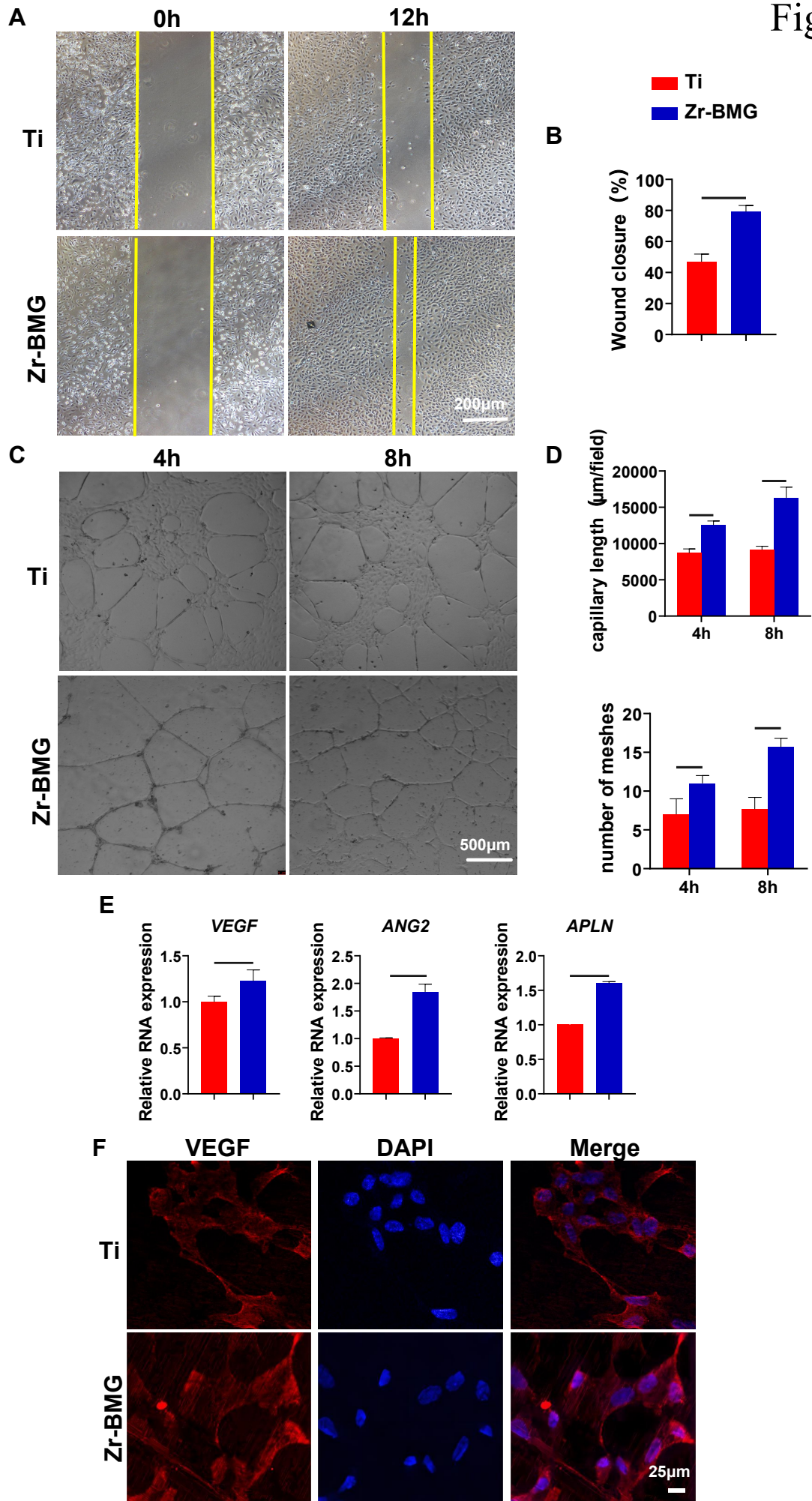


Figure 4 The angiogenesis reaction of different materials

- A. Scratch assay of HUVECs cultured in material's extract.
- B. Quantitative measurement of the scratch assay, indicating better wound healing in Ti and Zr-BMG. Scratch experiment images show that compared to Ti, HUVECs treated with Zr-BMG extract exhibited a faster migration speed.
- C. Representative images of tube formation assay at 4h and 8h.
- D. Quantitative measurement of the tube formation assay, indicating that Zr-BMG could efficiently promote vasculature development.
- E. qRT-PCR of angiogenesis marker, VEGF, ANG2 and APLN.
- F. Immunofluorescent staining of VEGF, confirming that Zr-BMG up-regulated the protein level of VEGF in comparison with Ti.

Data are presented as mean \pm SD. * p <0.05, ** p <0.01 and *** p <0.001.

Figure 5

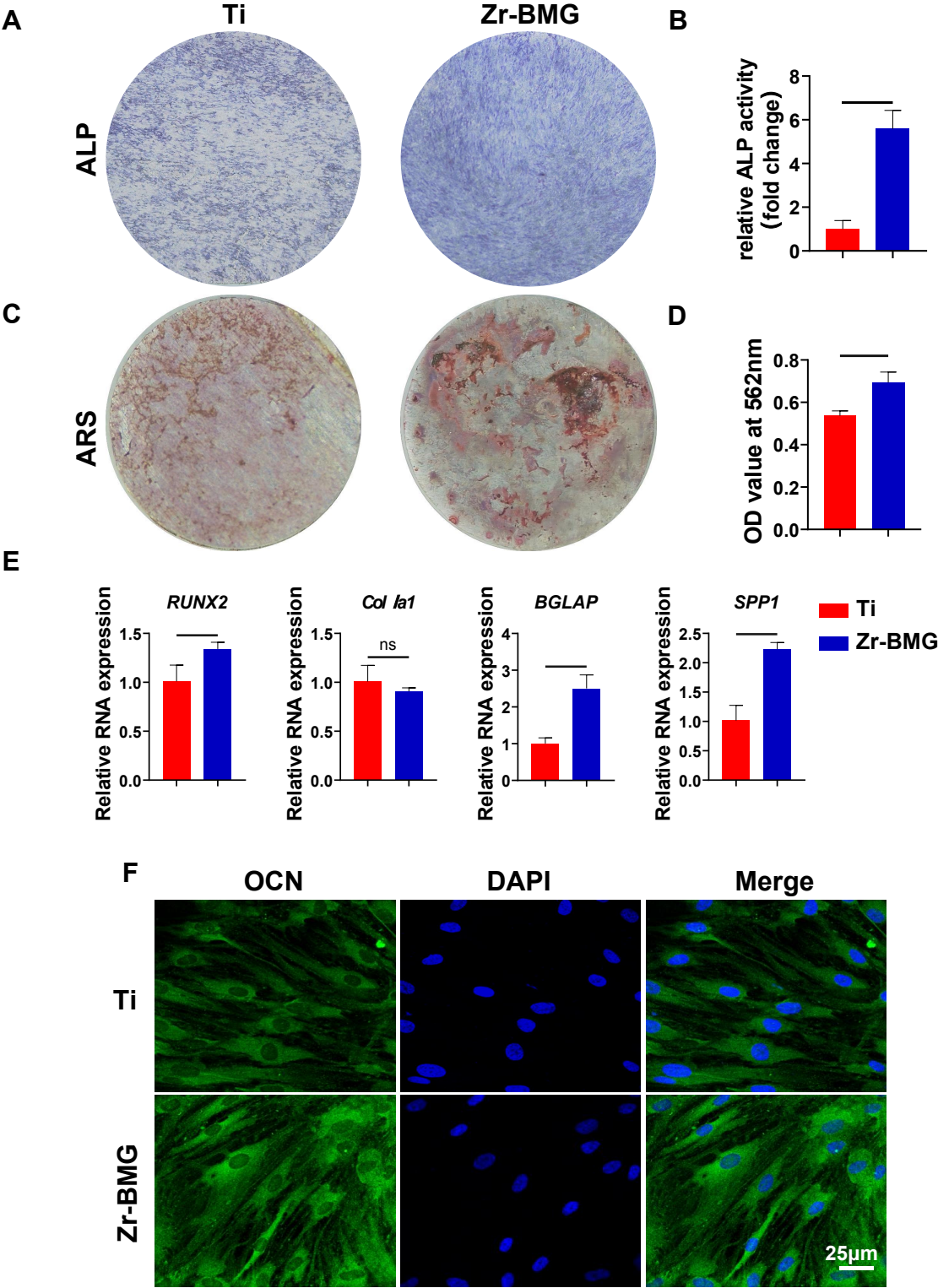


Figure 5 The osteogenic potential of different materials.

A. The Alkaline Phosphatase (ALP) staining images of hJBMMSCs after osteogenic induction on the material surface.

B. Quantitative measurement of ALP activity. Zr-BMG showed enhanced ALP activity.

C. The Alizarin Red S (ARS) staining images of hJBMMSCs seeded on the material surfaces after osteogenic induction.

D. Dissolved ARS OD value measured at 562nm. Zr-BMG showed exhibited better calcium nodules formation.

E. qRT-PCR of osteogenic markers. Zr-BMG significantly increased the expression of RUNX2, OCN and OPN.

F. Immunofluorescent staining of OCN confirming that Zr-BMG up-regulated the protein level of OCN in comparison with Ti.

Data are presented as mean \pm SD. * p <0.05, ** p <0.01 and *** p <0.001.

Figure 6

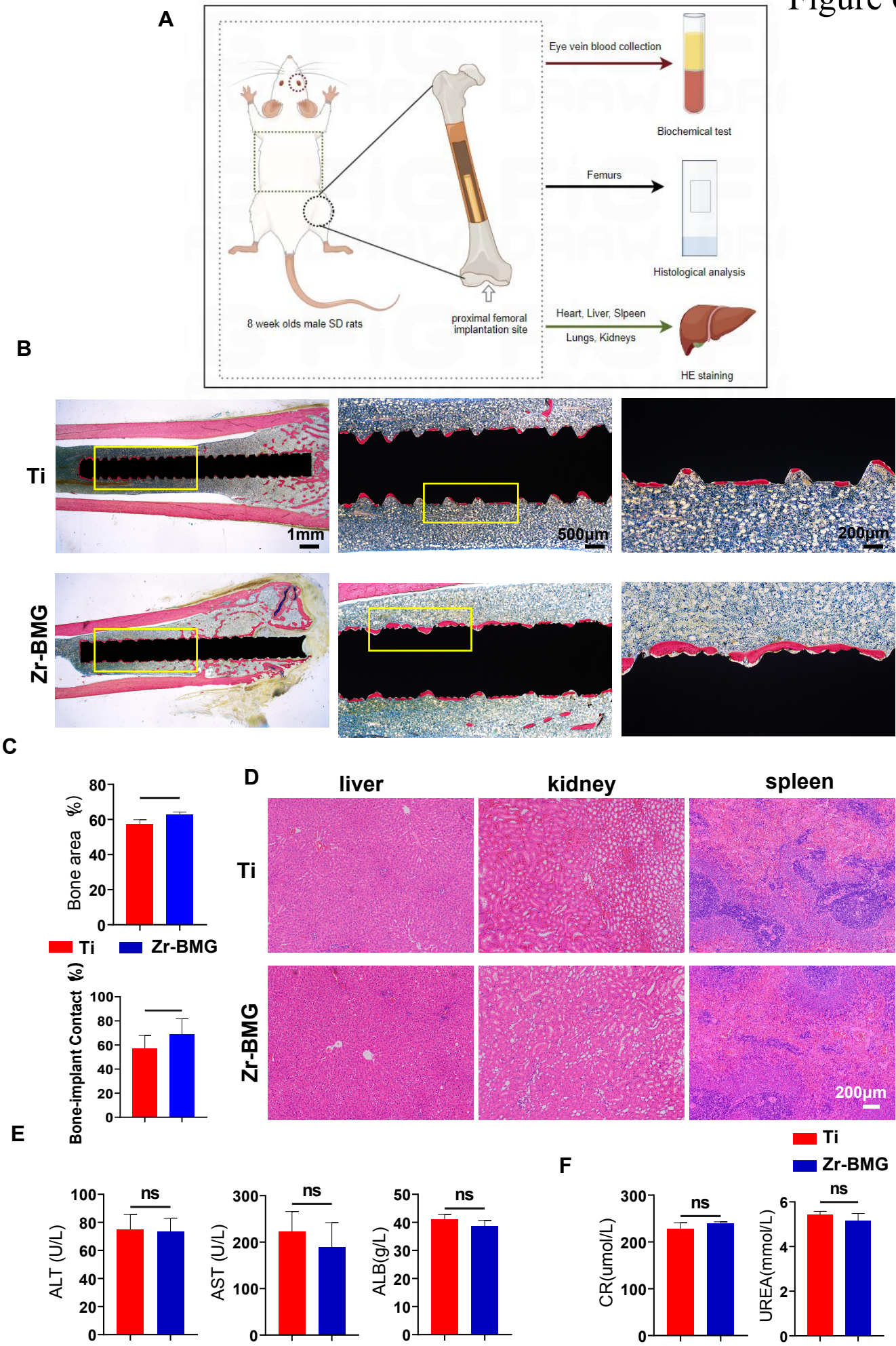


Figure 6. *In vivo* osteogenic potential of materials

A. The flow chart of *in-vivo* measurement.

B. Representative images of Stevenel's blue and Van Gieson's picrofuchsin staining showing new bone formation around implants. Zr-BMG implants were able to induce more bone formation that was in direct close contact to implant surfaces.

C. Quantitative measurement of bone area percentage around implants and relative bone-implant-contact length. Zr-BMG implants achieved better osseointegration than Ti.

D. H&E staining of liver, kidney and spleens sections, showing no obvious pathological change.

E. Biochemical parameters in animals with the implanted Ti and Zr-BMG.

Data are presented as mean \pm SD. * $p<0.05$, ** $p<0.01$ and *** $p<0.001$.

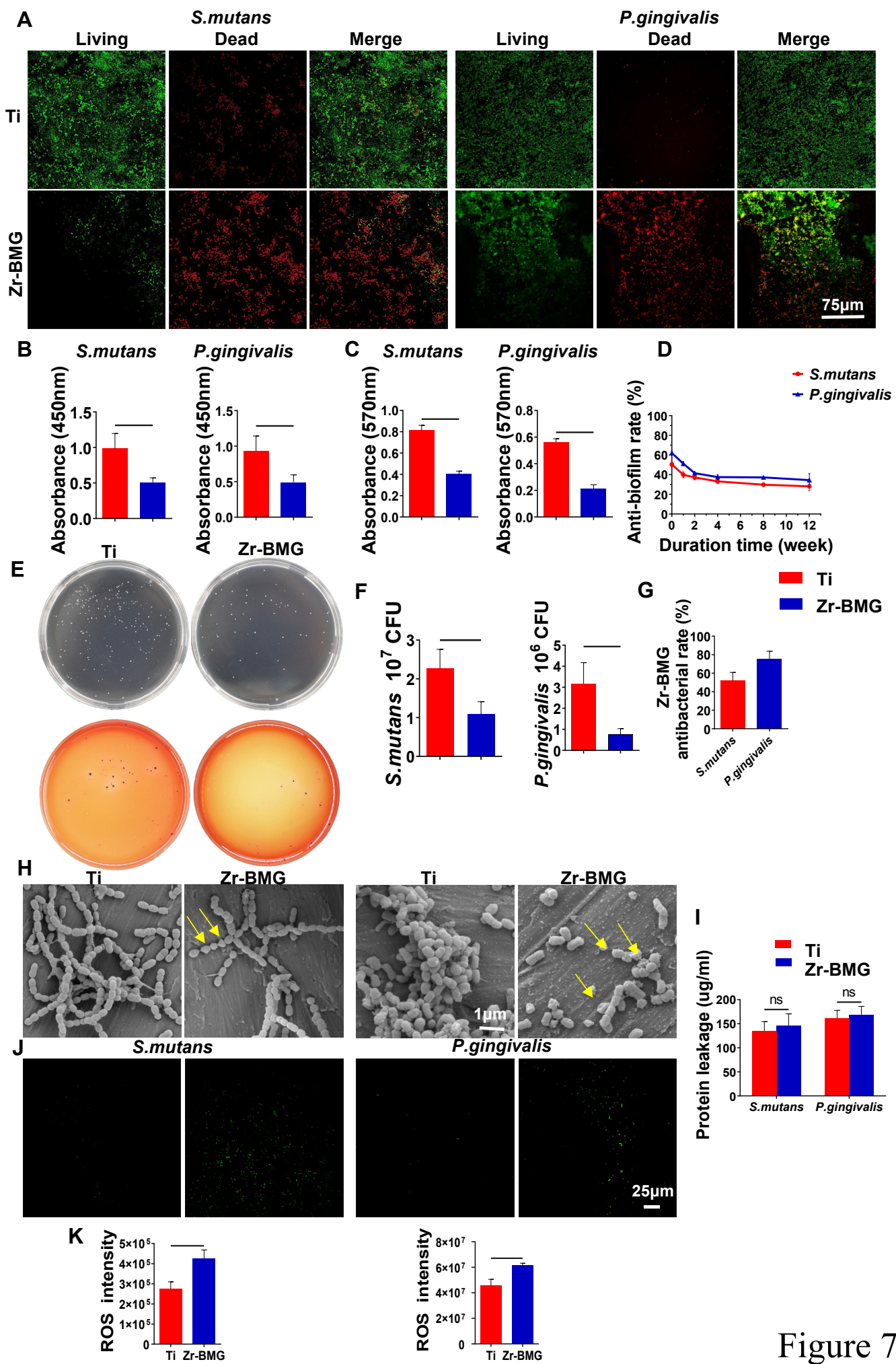


Figure 7

Figure 7 Antibacterial properties and mechanism

A. The live/dead staining images of *S.m* and *P.g* seeded on the surfaces of the two materials.

B. Quantitative measurement of fluorescence intensity. There were more dead bacteria and less live bacteria inoculated on Zr-BMG.

C. XTT assay of the bacterial activity on the surfaces of the two materials. The absorbance values of bacteria on Zr-BMG surface were lower than Ti.

D. The images of the dilution plate after co-culturing bacteria with the two materials (black colonies for *P.g* and yellow-white colonies for *S.m*).

E. Quantitative analysis of colonies. Compared to Ti, the quantity of both live bacteria adhering to Zr-BMG is significantly reduced.

F. The bactericidal rate of Zr-BMG against *P.g* is $(75.56 \pm 4.74)\%$, and for *S.m*, the bactericidal rate is $(51.96 \pm 5.13)\%$, indicating that Zr-BMG has a stronger killing ability against *P.g*.

G. The result of crystal violet staining. The removal efficiency of Zr-BMG on bacterial biofilm initially decreased rapidly, gradually stabilizing from the 2nd to 4th week.

H. Representative scanning electron microscope (SEM) images of *S.m* and *P.g* inoculated on the surfaces of the two materials. The bacterial cells inoculated on the surface of Zr-BMG exhibited a large number of cell wall ruptures, membrane fractures, and blurred or unclear cytoplasm with overflow.

I. The bacterial protein release levels after inoculation with *S.m* and *P.g* on two materials. The bacterial protein release levels on Zr-BMG are slightly higher, but there is no significant difference between the two.

J. Image of the ROS staining of free-released reactive oxygen species (ROS) in the bacterial suspension after inoculation with *S.m* and *P.g* on the two materials.

K. Fluorescence intensity of ROS. The Zr-BMG induced substantial ROS production in bacteria, elevating intracellular ROS levels.

Data are presented as mean \pm SD. * $p < 0.05$, ** $p < 0.01$ and *** $p < 0.001$.